“Biomimetic assembly and activation of [FeFe]-hydrogenases“ G. Berggren, A. Adamska, C. Lambertz, T. R. Simmons, J. Esselborn, M. Atta, S. Gambarelli, JM Mouesca, E. Reijerse, W. Lubitz, T. Happe, V.Artero, M. Fontecave*; *Nature*, **2013**, 499, 66-69. DOI: 10.1038/nature12239 http://www.nature.com/nature/journal/v499/n7456/full/nature12239.html

# SUPPLEMENTARY INFORMATION

for

# Biomimetic assembly and activation of [FeFe]-hydrogenases

G. Berggren[1,2¥], A. Adamska[3#], C. Lambertz[4#], T. Simmons[1#], J. Esselborn[4], M. Atta[1], S. Gambarelli[5], JM Mouesca[5], E. Reijerse[3], W. Lubitz[3], T. Happe[4], V.Artero[1], M. Fontecave[1,2]*

[1] Laboratoire de Chimie et Biologie des Métaux (CEA / Université Grenoble 1 / CNRS), 17 rue des Martyrs, F-38054 Grenoble cedex 9, France

[2] Collège de France, 11 place Marcelin-Berthelot, F-75231 Paris cedex 5, France.

[3] Max-Planck-Institut für Chemische Energiekonversion, Stiftstrasse 34–36, 45470 Mülheim an der Ruhr, Germany.

[4] Lehrstuhl Biochemie der Pflanzen, AG Photobiotechnologie, Ruhr Universität Bochum, Universitätsstrasse 150, 44801 Bochum, Germany.

[5] CEA, INAC, LCIB (UMR-E 3 CEA / UJF-Grenoble 1), 17 rue des Martyrs, F-38054 Grenoble CEDEX 9, France

[#] these authors equally contributed to the present study

[¥] Current address : Dept. of Biochemistry & Biophysics, Stockholm University, Svante

Arrhenius väg 16, 106 91 Stockholm, Sweden

## Synthesis

**$(Et_4N)_2[Fe_2(pdt)(CO)_4(CN)_2]$ (1):** $(Et_4N)CN$ (0.16 g, 1.00 mmol) was dissolved in MeCN (5 mL) and added *via* cannula to a solution of $[Fe_2(pdt)(CO)_6]$ [1] (0.15 g, 0.40 mmol) in MeCN (5 mL) under argon. The reaction mixture was stirred for 2 hours at room temperature to give a dark red solution. The solvent was removed under reduced pressure to give a dark red oily residue. This was dissolved in acetone (10 mL) and filtered *via* cannula to give a dark red filtrate. The solution was mixed with EtOAc (10 mL) and cooled to –26 ºC to give $(Et_4N)_2$**1** as a deep red crystalline solid (0.22 g, 85%) $\nu_{max}/cm^{-1}$ (acetonitrile) 2076, 1964, 1922, 1884, 1873 (sh) (CO).

**$(Et_4N)_2[Fe_2(pdt)(CO)_4(^{13}CN)_2]$:** K ($^{13}$CN) (0.05 g, 0.80 mmol) was dissolved in MeOH (5 mL) and added *via* cannula to a solution of $[Fe_2(pdt)(CO)_6]$ [1] (0.15 g, 0.40 mmol) in MeCN (5 mL) under Argon. The reaction mixture was stirred for 2 hours at room temperature to give a dark red solution. $(Et_4N)Br$ (0.20 g, 0.95 mmol) was dissolved in MeCN (10 mL) and added to the reaction mixture, which was stirred for a further 30 minutes. The solvent was removed under reduced pressure to give a dark red oily residue. This was dissolved in acetone (10 mL) and filtered *via* cannula to give a dark red filtrate. The solution was mixed with EtOAc (20 ml) and cooled to –26 ° to give $(Et_4N)_2[Fe_2(pdt)(CO)_4(^{13}CN)_2]$ as a deep red solid (0.18 g, 72%) $\nu_{max}/cm^{-1}$ (acetonitrile) 2032 ($^{13}$CN), 1963, 1922, 1885, 1871(sh) (CO).

**$(Et_4N)_2[Fe_2(odt)(CO)_4(CN)_2]$ (3)** $(Et_4N)CN$ (0.08 g, 0.50 mmol) was dissolved in MeCN (5 ml) and added *via* cannula to a solution of $[Fe_2(odt)(CO)_6]$ [2] (0.10 g, 0.25 mmol) in MeCN (10 ml) under argon. The reaction mixture was stirred for 2 hours at room temperature to give a dark red solution. The solvent was removed under reduced pressure to give a dark red oily residue. This was dissolved in acetone (10 ml) and filtered *via* cannula to give a dark red filtrate. The solution was mixed with EtOAc (10 ml) and cooled to -26 ºC to give $(Et_4N)_2$**3** as a deep red crystalline solid (0.14 g, 88%) $\nu_{max}/cm^{-1}$ (acetonitrile) 2077, 1968, 1929, 1891, 1878 (sh) (CO).

## Supplementary discussion

### DFT calculations.

*Molecular models of the hybrid.* We modelled the three cysteine ligands of the [4Fe-4S] cluster of the hybrid as $EtS^{-}$ thiolate ligands, as is common practice. Consequently, the reduced cluster stands as a $[Fe_4\text{-}(\mu_3\text{-}S)_4(SEt)_3]^{2-}$ molecular anion (one iron ligand is yet vacant).

In all our DFT calculations, we kept the molecular integrity of the $[Fe_2]$ complex, $[Fe_2(pdt)(CO)_4(CN)_2]^{2-}$, constructed from $[Fe_2(pdt)(CO)_6]$ (CSD file md239) in which two of the neutral carbonyl ligands (one on each iron site) have been appropriately replaced by isoelectronic $CN^{-}$ ligands. The diiron $[Fe_2(pdt)(CO)_4(CN)_2]^{2-}$ complex is diamagnetic. Each iron site is low-spin S=0 (we verified computationally that this is indeed the case).

The full hybrid model thus assumes the following chemical formula: $([Fe_4(\mu_3\text{-}S)_4(SEt)_3].[Fe_2(pdt)(CO)_4(CN)_2])$ of total charge –4. We will consider in the following two bridging modes for the -C≡N- ligand: [4Fe-4S]-N≡C-$[Fe_2]$ (**model 1**) and [4Fe-4S]-C≡N-$[Fe_2]$ (**model 2**).

*Electronic/magnetic states of the [4Fe-4S] cluster***.** In its reduced state (S=1/2), the [4Fe-4S] cluster is made of a mixed-valence pair (of spin +9/2) antiferromagnetically coupled to a ferrous pair of spin -8/2 resulting into the S=1/2 ground state. There are therefore six possible spin alignments among the four iron atoms. As the spin-coupled S=1/2 state is not directly accessible through DFT mono-determinantal codes, one relies on the computation of spin-uncoupled broken symmetry (BS) states for which the magnetic quantum number $m_s=1/2$ is constrained while preserving local iron high spins[3]. We called them $BS_{ij} = BS_{12}$, $BS_{13}$, $BS_{14}$, $BS_{23}$, $BS_{24}$ and $BS_{34}$, respectively, where ‘ij’ refers to the ferrous pair (Table S2). Note that $Fe_4$ will always be the one linked to the diiron complex via the -C≡N- bridging ligand.

*Spin coupling procedure***.** For both $^{13}C$ and $^{14}N$ nuclei, DFT isotropic hyperfine coupling constants {A} are first computed for each *spin uncoupled* ($m_s=1/2$) BS states. These DFT quantities have to be *spin-coupled* in order to provide hyperfine couplings {a} for comparison with the experimental values. The correction for $^{13}C$ and $^{14}N$ coupling is the same because both nuclei belong to the same $CN^{-}$ ligand bound to the same cluster. Both DFT-computed {A} and predicted {a} quantities are related by $a = K(Fe)\,[A/(2S_{Fe})]$ where $2S_{Fe}$ is twice the local spin of $Fe_4$ (ferrous : $2S_{Fe} = 4$ and mixed-valence : $2S_{Fe} = 4.5$). K(Fe) is a spin-coupling coefficient linking the local spins [$S_{Fe}$] to the total spin S=1/2. For symmetric reduced S=1/2 [4Fe-4S](Cys)$_4$ clusters, experimentally-derived values would be the following[4]: $K(Fe^{2.5+}) \approx +1.5$ and $K(Fe^{2+}) \approx -1.0$ (with $\Sigma_{Fe}$ K(Fe) = 1).

In practice, these {K(Fe)} values would result in a ≈ A/3 if $Fe_4$ belongs to the mixed-valence pair, and a ≈ A/4 if $Fe_4$ belongs to the ferrous pair. In the present case however, $Fe_4$ is bound to a cyanide bridging ligand, and the exact {K(Fe)} values in such an asymmetric case are unknown. The above corrections leading from {A} to {a} are thus tentative. In Tables S3 and S4, we also compute the ratio $A_{^{13}C}/A_{^{14}N}$, which simply turns out to be equal to $a_{^{13}C}/a_{^{14}N}$ as both nuclei are borne by the same iron atom. This ratio is moreover independent from the spin-coupling procedure and will therefore serve as a more reliable guide. Let us recall here that, experimentally: $|a_{^{13}C}| \approx 4$ MHz, $|a_{^{14}N}| < \approx 1$ MHz. We therefore expect: $a_{^{13}C}/a_{^{14}N} > \approx 4$.

*DFT calculations of hyperfine coupling constants***.** We relied on the electronic structures and the subsequent hyperfine coupling constants computed by the ADF2012 density functional code[5]. Both hybrid **models 1** and **2**, each in the six possible broken symmetry states**,** have been fully geometry-optimized *in vacuo* using the standard VBP potential, i.e. Wilk, Vosko and Nusair functional[6], completed by Becke correction for the exchange[7] and Perdew correction for the correlation[8].

All hyperfine couplings' calculations were performed using the PBE0 exchange-correlation potential[9], a parameter-free density functional model whose results regarding spectroscopic properties are close to those computed by heavily parameterized functionals. For the second hybrid **model 2** [4Fe-4S cluster]-C≡N-[$Fe_2$] and for the first $BS_{12}$ broken symmetry state we have compared the carbon and nitrogen PBE0 hyperfine values (Table S3) to those computed first with the *local* VBP potential and for two *non-local* potentials. One is the standard B3LYP potential[10] (mixing in 20% of the pure Hartree-Fock (HF) exchange) and the other is a variant thereof mixing in only 5% of HF exchange, presented[11] as being suitable to describe metal-ligand (i.e. iron-sulfur) covalency within iron-sulfur clusters (data presented in Table S4).

Finally, triple-zeta + two polarization functions have been used for all atoms (TZ2P basis set in SCM-ADF nomenclature). Moreover, when estimating hyperfine coupling constants, no frozen core approximation has been set allowing all s atomic functions to be fully polarized as is required.

The computed isotropic hyperfine coupling values for both **models 1** and **2**, each in the six possible BS states, are presented in Tables S3 and S4, respectively. For **model 1**, when $Fe_4$ belongs to the delocalized mixed-valence pair (as for the first three BS states of Table S2, for $BS_{12}$, $BS_{13}$ and $BS_{23}$), we found on the average that $A_{^{13}C} \approx 20.5$ MHz and $A_{^{14}N} \approx 15.6$ MHz, that is $a_{^{13}C} \approx 6.8$ MHz and $a_{^{14}N} \approx 5.2$ MHz, with $a_{^{13}C} /a_{^{14}N} \approx 1.31$. The nitrogen hyperfine coupling is much too large, and the ratio $a_{^{13}C} /a_{^{14}N}$ too small to be compatible with the experiment.

For **model 1**, when $Fe_4$ now belongs to the ferrous pair (as for the last three BS states of Table S2, for $BS_{14}$, $BS_{24}$ and $BS_{34}$), we found on the average $A_{^{13}C} \approx -20.9$ MHz and $A_{^{14}N} \approx -9.9$ MHz, that is $a_{^{13}C} \approx 5.3$ MHz and $a_{^{14}N} \approx 2.5$ MHz, with $a_{^{13}C} /a_{^{14}N} \approx 2.11$. The nitrogen hyperfine coupling is still large, and the ratio $a_{^{13}C} /a_{^{14}N}$ still too small to be fully compatible with experiment.

The gyromagnetic ratios of $^{13}C$ and $^{14}N$ nuclei are in the 3.5 ratio (1.4/0.4). All other things being equal, we would therefore expect the computed hyperfine coupling constants $A_{^{13}C}$ and $A_{^{14}N}$ to be in that ratio. This is not the case, even though both nuclei are linked via a triple bond. In other words, the spin density of the nucleus closest to the iron ion (here, the nitrogen) is more affected than that of the other (carbon) nucleus. It can be seen in Table S2 that, indeed, the magnitude of $A_{^{13}C}$ does not vary much as a function of the formal iron valence (2.5+ or 2+). That of $A_{^{14}N}$ is reduced from 16 MHz to 9.8 MHz, thus by 6.2 MHz. We will come back to that last value below.

For **model 2**, with $Fe_4$ belonging to the ferrous pair (as for the last three BS states of Table S3, for $BS_{14}$, $BS_{24}$ and $BS_{34}$), we found on average that $A_{^{13}C} \approx -2.4$ MHz and $A_{^{14}N} \approx -8.0$ MHz, that is $a_{^{13}C} \approx -0.4$ MHz and $a_{^{14}N} \approx 2.0$ MHz, with $a_{^{13}C} /a_{^{14}N} \approx 0.30$. The carbon hyperfine coupling is now too small, which excludes this possibility.

Finally, for **model 2**, when $Fe_4$ now belongs to the delocalized mixed-valence pair (as for the first three BS states of Table S3, for $BS_{12}$, $BS_{13}$ and $BS_{23}$), we found on average that $A_{^{13}C} \approx 25.8$ MHz and $A_{^{14}N} \approx 7.7$ MHz, that is $a_{^{13}C} \approx 8.6$ MHz and $a_{^{14}N} \approx 2.6$ MHz, with $a_{^{13}C} /a_{^{14}N} \approx 3.4$ (even 3.85 in the case of $BS_{13}$). Although the PBE0 potential exaggerates the magnitudes of the couplings, the computed values (and their ratio) are satisfyingly compatible with the experiment. The dependence of the computed hyperfine coupling constants on the choice of the exchange-correlation potential is illustrated in Table S5.

As for **model 1**, the magnitudes of the hyperfine coupling constants computed for the nucleus further away from the iron ion (here, the nitrogen) cluster around a value of 8 MHz. In contrast, those corresponding to the closest nucleus (here, the carbon) are drastically reduced from 25.8 MHz (mixed-valence $Fe_4$) down to 2.4 MHz (ferrous $Fe_4$). This represents an average reduction by 23.4 MHz. In the same position (closest to the iron) we had 6.2 MHz for the nitrogen nucleus. These two values (23.4 and 6.2) are indeed proportional to the nuclear gyromagnetic ratios 1.4 and 0.4, respectively. Both carbon and nitrogen nuclei, when directly linked to $Fe_4$, are therefore equally affected by the nearby change from mixed-valence to ferrous.

We conclude this theoretical section by stating that the experimental data are compatible with the presence of a cyanide ion bridging both the [4Fe-4S] cluster and the [$Fe_2$] complex according to **model 2**: [4Fe-4S cluster]-C≡N-[$Fe_2$], more specifically with $Fe_4$ belonging to the mixed-valence (i.e. being formally $Fe^{2.5+}$).

*Simulation of IR spectra*. Within the IR module of the ADF2012-DFT code, there are two ways to compute IR transitions, one (analytical) being 3 to 5 times faster than the other one (numerical). The choice of the analytical procedure restricts that of the exchange-correlation potentials compatible with that module. We therefore proceeded to various tests in order to calibrate our method : (i) for CO and $CN^-$ in solution (target experimental values: 2143 $cm^{-1}$ and 2080 $cm^{-1}$, respectively, in water[12]); (ii) for complex **1** in solution (target experimental values : 1914 $cm^{-1}$, 1950 $cm^{-1}$ and 1981 $cm^{-1}$ for the CO ligands, and a massif centred around 2052 $cm^{-1}$ for the $CN^-$ ligands; see Figure 2A of main text). The exchange-correlation potential of choice turned out to be the one modelling the Stoll treatment of correlation[13]. The IR simulation required full geometry-reoptimization of the systems for that potential, in solution (dielectric constant $\varepsilon = 78$ for the whole calibration procedure), followed by the IR module at the optimized geometry. The results of the calibration are presented in Table S6. As can be seen there, the experimental values are quite well reproduced by the proposed DFT procedure.

For hybrids, and because of the computation time necessary for precise calculations, we chose a test case, that of one of our three candidates for **1**-HydF, that is the [4Fe-4S]-C≡N-[$Fe_2$] hybrid called $BS_{12}$ in Table S4 (experimental values reported in Figure 2B for **1**-HydF). Its geometry has been fully-reoptimized with the Stoll potential within a continuum dielectric constant of $\varepsilon = 4$ (mimicking the average polarizing effect of the protein matrix) and its IR stretching frequencies calculated as above. It has to be noticed that the calculated frequencies for the charged $CN^-$ ion are more sensitive to solvation/protein environment than those for the neutral CO molecule. Plotting the vibration frequency as a function of $(1-1/\varepsilon)$ yields a slope of 6 $cm^{-1}$ for CO against 37 $cm^{-1}$ for $CN^-$.

## Supplementary tables

**Table S1**. FTIR data recorded for the hybrid protein **1**-HydF and complex **1**. Values reported for as-isolated samples of CaHydF containing the natural co-factor are shown for comparison.

| **Sample** | **Frequencies (cm$^{-1}$)** |
|---|---|
| CaHydF isolated from *C. acetobutylicum*[14] | 2069(w), 2044(m), 1967(w), 1943(s), 1907(m), 1877(m) |
| CaHydF isolated from *E. coli* expressing the maturation system[15] | 2046(m), 2027(m), 1940 (s), 1881(m) |
| **1**-HydF | 2055(w), 2038(m), 1968(w), 1943(s), 1987 (bs) |
| **1** | 2052, 1981, 1950, 1914 |

**Table S2.** Formal iron valences and spin alignment in the various Electronic/magnetic states of the [4Fe-4S] cluster

| **BS states**[a] | **Formal iron valences & spin alignment**[b] |
|---|---|
| $BS_{12}$ | $Fe^{2+}(\downarrow)$- $Fe^{2+}(\downarrow)$- $Fe^{2.5+}(\uparrow)$- $Fe^{2.5+}(\uparrow)$ |
| $BS_{13}$ | $Fe^{2+}(\downarrow)$- $Fe^{2.5+}(\uparrow)$- $Fe^{2+}(\downarrow)$- $Fe^{2.5+}(\uparrow)$ |
| $BS_{23}$ | $Fe^{2.5+}(\uparrow)$- $Fe^{2+}(\downarrow)$- $Fe^{2+}(\downarrow)$- $Fe^{2.5+}(\uparrow)$ |
| $BS_{14}$ | $Fe^{2+}(\downarrow)$- $Fe^{2.5+}(\uparrow)$- $Fe^{2.5+}(\uparrow)$- $Fe^{2+}(\downarrow)$ |
| $BS_{24}$ | $Fe^{2.5+}(\uparrow)$- $Fe^{2+}(\downarrow)$- $Fe^{2.5+}(\uparrow)$- $Fe^{2+}(\downarrow)$ |
| $BS_{34}$ | $Fe^{2.5+}(\uparrow)$- $Fe^{2.5+}(\uparrow)$- $Fe^{2+}(\downarrow)$- $Fe^{2+}(\downarrow)$ |

(a) Each Broken Symmetry (BS) state is described by a label ('12', '13', etc.) indicating which iron pair is ferrous. (b) In the order $Fe_1$-$Fe_2$-$Fe_3$-$Fe_4$.

**Table S3.** DFT computed $^{13}C$ and $^{14}N$ {A} hyperfine coupling constants

| **[4Fe-4S]-N≡C-[Fe$_2$]** | | | | |
|---|---|---|---|---|
| BS states[a] | E(eV)[b] | $A_{^{14}N}$ (MHz) | $A_{^{13}C}$ (MHz) | $A_{^{13}C}/A_{^{14}N}$[c] |
| $BS_{12}$ | -450.079 | +15.1 | +20.4 | 1.35 |
| $BS_{13}$ | -449.913 | +17.0 | +20.3 | 1.19 |
| $BS_{23}$ | -450.032 | +14.8 | +20.8 | 1.41 |
| *average* | | ***+15.6*** | ***+20.5*** | ***1.31*** |
| $BS_{14}$ | -450.127 | -9.9 | -21.0 | 2.12 |
| $BS_{24}$ | -450.103 | -10.1 | -20.8 | 2.06 |
| $BS_{34}$ | -450.112 | -9.7 | -20.9 | 2.15 |
| *average* | | ***-9.9*** | ***-20.9*** | ***2.11*** |

(a) Each Broken Symmetry (BS) state is described by a label ('12', '13', etc.) indicating which iron pair is ferrous. $Fe_4$ is the one bearing the cyanide bridging ligand. (b) Bonding energies (eV) computed for the optimized geometries. (c) This ratio is independent from the spin-coupling procedure (i.e. $A_{^{13}C}/A_{^{14}N} = a_{^{13}C}/a_{^{14}N}$).

**Table S4** DFT computed $^{13}C$ and $^{14}N$ {A} hyperfine coupling constants

| **[4Fe-4S]-C≡N-[Fe$_2$]** | | | | |
|---|---|---|---|---|
| BS states[a] | E(eV)[b] | $A_{^{14}N}$ (MHz) | $A_{^{13}C}$ (MHz) | $A_{^{13}C}/A_{^{14}N}$[c] |
| $BS_{12}$ | -449.555 | +7.5 | +23.3 | 3.11 |
| $BS_{13}$ | -449.489 | +7.8 | +30.0 | 3.85 |
| $BS_{23}$ | -449.523 | +7.8 | +24.0 | 3.08 |
| *average* | | ***+7.7*** | ***+25.8*** | ***3.35*** |
| $BS_{14}$ | -449.642 | -7.9 | -2.6 | 0.33 |
| $BS_{24}$ | -449.658 | -8.1 | -2.0 | 0.25 |
| $BS_{34}$ | -449.642 | -8.0 | -2.7 | 0.34 |
| *average* | | ***-8.0*** | ***-2.4*** | ***0.30*** |

(a) Each Broken Symmetry (BS) state is described by a label ('12', '13', etc.) indicating which iron pair is ferrous. $Fe_4$ is the one bearing the cyanide bridging ligand. (b) Bonding energies (eV) computed for the optimized geometries. (c) This ratio is independent from the spin-coupling procedure (i.e. $A_{^{13}C}/A_{^{14}N} = a_{^{13}C}/a_{^{14}N}$).

**Table S5** DFT computed $^{13}$C and $^{14}$N {A} hyperfine coupling constants

| **[4Fe-4S]-C≡N-[Fe$_2$]** | | | |
|---|---|---|---|
| XC potential[a] | $A_{^{14}N}$ (MHz) | $A_{^{13}C}$ (MHz) | $A_{^{13}C}/A_{^{14}N}$[b] |
| VBP | +6.9 | +10.6 | **1.53** |
| PBE0 | +7.5 | +23.3 | **3.11** |
| B3LYP (5% HF) | +9.2 | +27.5 | **2.99** |
| B3LYP (20% HF) | +9.3 | +35.3 | **3.80** |

These calculations are performed for the BS$_{12}$ state. (a) Exchange-correlation (XC) potential (see main text of the methods summary). (b) This ratio is independent from the spin-coupling procedure (i.e. $A_{^{13}C}/A_{^{14}N} = a_{^{13}C}/a_{^{14}N}$).

**Table S6**. DFT-computed versus experimental CO and CN$^-$ IR stretching frequencies (cm$^{-1}$).

| Systems | Method | CO | CN$^-$ |
|---|---|---|---|
| Isolated[a] | Exp[c]. | **2143** | **2080** |
| | DFT | *2148* | *2078* |
| [Fe$_2$]<br>Complex[a] | Exp[d]. | **1914**<br>**1950**<br>**1981** | **2052** |
| | DFT | *1904, 1910*<br>*1946*<br>*1961* | *2066*<br>*2071* |
| [4Fe-4S]-C≡N-[Fe$_2$]<br>Hybrid[b] | Exp[e]. | **1897**<br>**1943**<br>**1968** | **2038**<br>**2055** |
| | DFT | 1886, 1894<br>1944<br>1958 | 2010[f]<br>2060[g] |

(a) ε = 78; (b) ε = 4; (c) ref 23; (d) From Figure 2A for complex **1**; (e) From Figure 2B for **1**-HydF; (f) bridging CN$^-$; (g) terminal CN$^-$.

## Supplementary figures

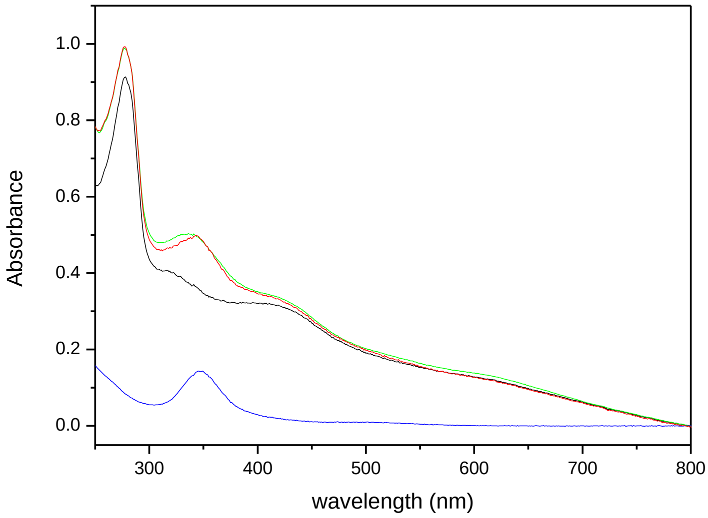

**Figure S1a**. **UV/Vis spectra of 1-HydF in Tris-HCl buffer (50 mM, 150 mM NaCl, pH 8).** **1**-HydF (20 µM, red line); the HydF protein (20 µM, black line); complex **1** (20 µM, blue line); Calculated spectrum obtained through mathematical addition of **1** and HydF spectra in a 1:1 ratio (20 µM, green line)

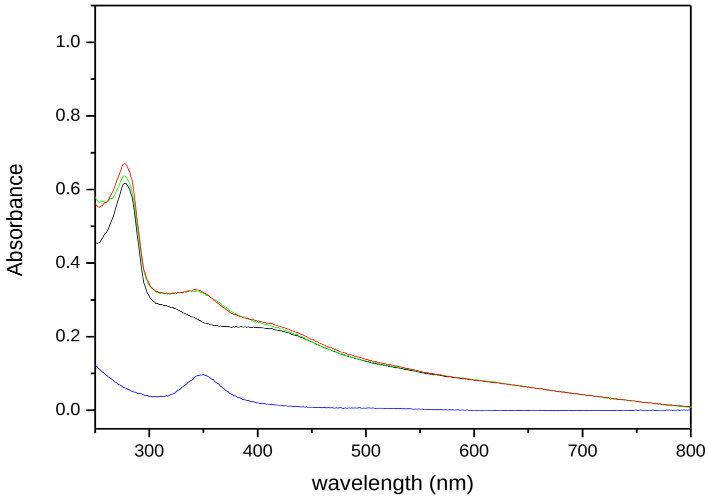

**Figure S1b**. **UV/Vis spectra of 2-HydF in Tris buffer (50 mM, 150 mM NaCl, pH 8). 2-**HydF (14 µM, red line); the HydF protein (14 µM, black line); complex **2** (14 µM, blue line); Calculated spectrum obtained through mathematical addition of **2** and HydF spectra in a 0.95:1 ratio (14 µM, green line)

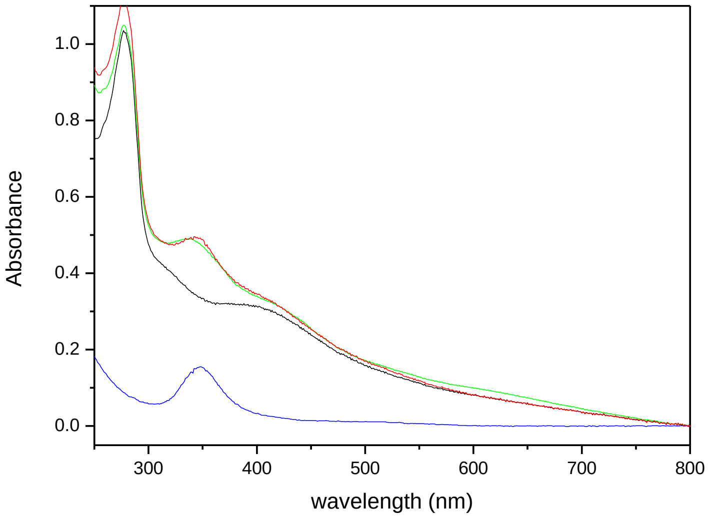

**Figure S1c. UV/Vis spectra of 3-HydF in Tris buffer (50 mM, 150 mM NaCl, pH 8). 3-**HydF (20 µM, red line); the HydF protein (20 µM, black line); complex **3** (20 µM, blue line); Calculated spectrum obtained through mathematical addition of **3** and HydF spectra in a 1:1 ratio (20 µM, green line)

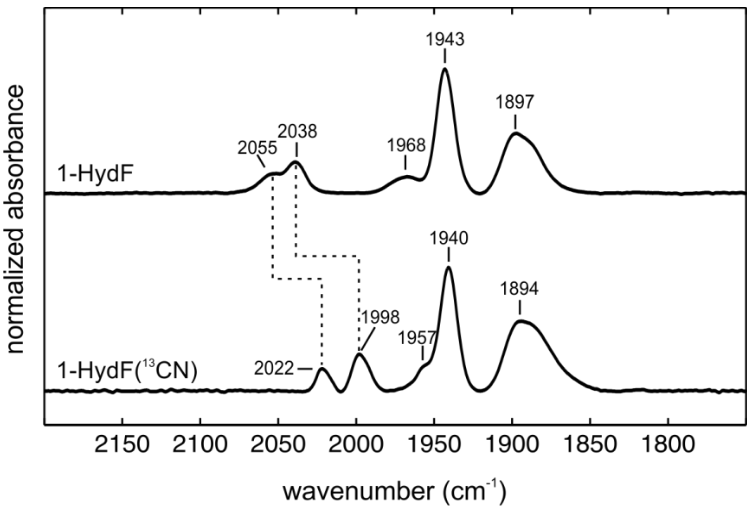

**Figure S2.** Solution Fourier-transform infrared spectra of **1**-HydF in solution with $^{12}$CN and $^{13}$CN ($^{13}$C labelled cyanide ligands in **1**) recorded in HEPES buffer (20 mM, 100 mM KCl, pH 7.5).

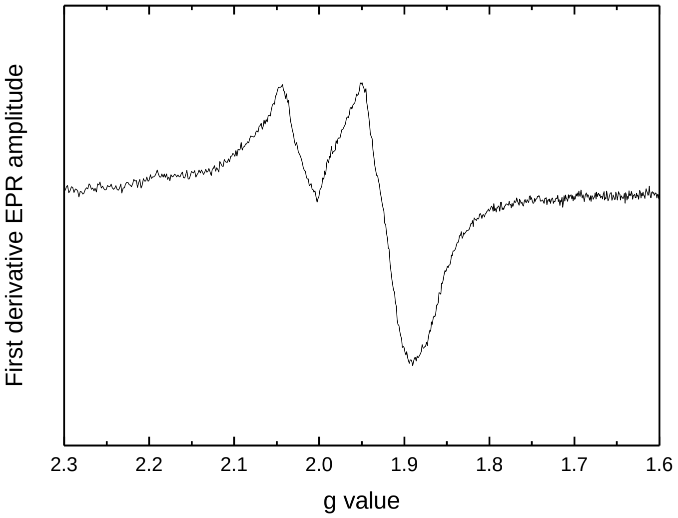

**Figure S3a: Continuous wave EPR spectrum of 2-HydF.** X-band EPR spectrum recorded at 10K for dithionite-reduced **2**-HydF in Tris-HCl buffer (50 mM, 150 mM NaCl, $Na_2S_2O_4$ 5 mM, pH 8). Microwave power = 100 µW, mod. amp. = 1 mT, mwfreq. = 9.65 GHz..

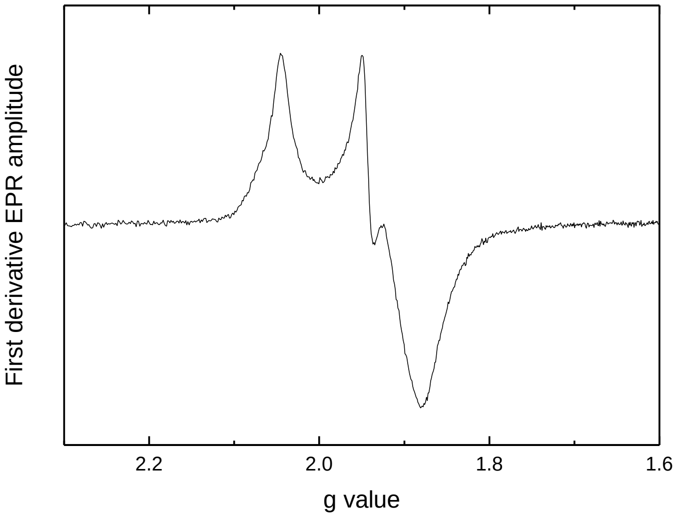

**Figure S3b: Continuous wave EPR spectrum of 3-HydF.** X-band EPR spectrum recorded at 10K for dithionite-reduced **3**-HydF in Tris-HCl buffer (50 mM, 150 mM NaCl, $Na_2S_2O_4$ 5 mM, pH 8). Microwave power = 100 µW, mod. amp. = 1 mT, mwfreq. = 9.65 GHz. On the basis of its power saturation behaviour at 10K, the contribution observed at g = 1.90 and corresponding to only a few percent of the total signal intensity is assigned to a small fraction of residual HydF lacking the synthetic co-factor.

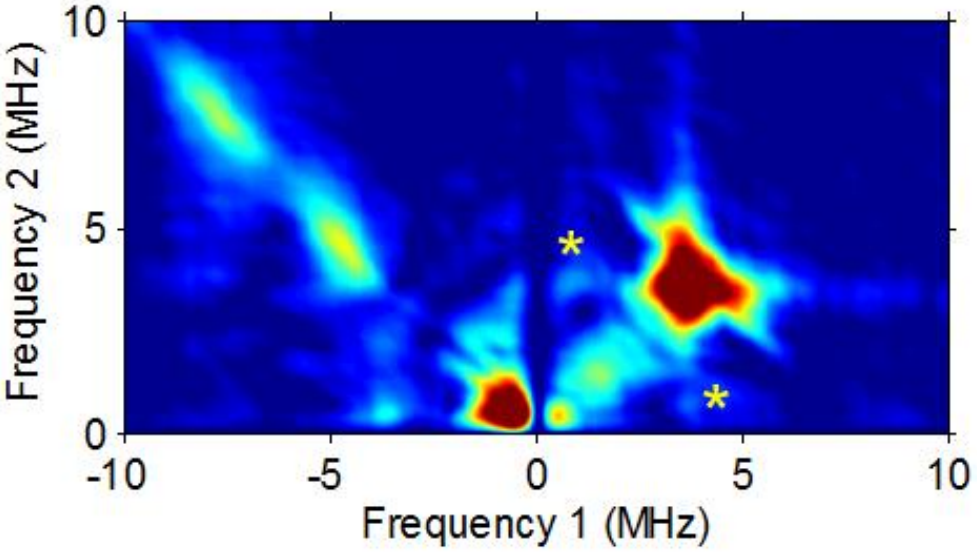

**Figure S4:** X-band HYSCORE spectrum of $^{13}CN^{-}$-labelled **1**-HydF recorded at B=360 mT (corresponding to $g_{\perp}$) and T=8K (see above for more details). The antidiagonal ridge centered around 3.6 MHz in the (+,+) quadrant is attributed to $^{13}C$ hyperfine coupling. It is much more visible on the CF-NF experiment displayed in Figure 3. The other features noted by asterisks (*) in this quadrant can be attributed to a weakly coupled $^{14}N$ nucleus. While CF-NF (Figure 3) and HYSCORE (this figure) provide essentially the same information, the former is more sensitive for disordered system[16]. It correlates the combination frequencies ($\nu_{\alpha}+\nu_{\beta}$) in one direction with the nuclear frequencies ($\nu_{\alpha}$ and $\nu_{\beta}$ ) in the other direction. This means that, to first order, a small hyperfine tensor for an I=1/2 spin is detected as a straight horizontal line in the (+,+) quadrant. HYSCORE correlates nuclear frequencies in the two directions and so displays a small hyperfine tensor for an I=1/2 spin as an antidiagonal ridge in the (+,+) quadrant.

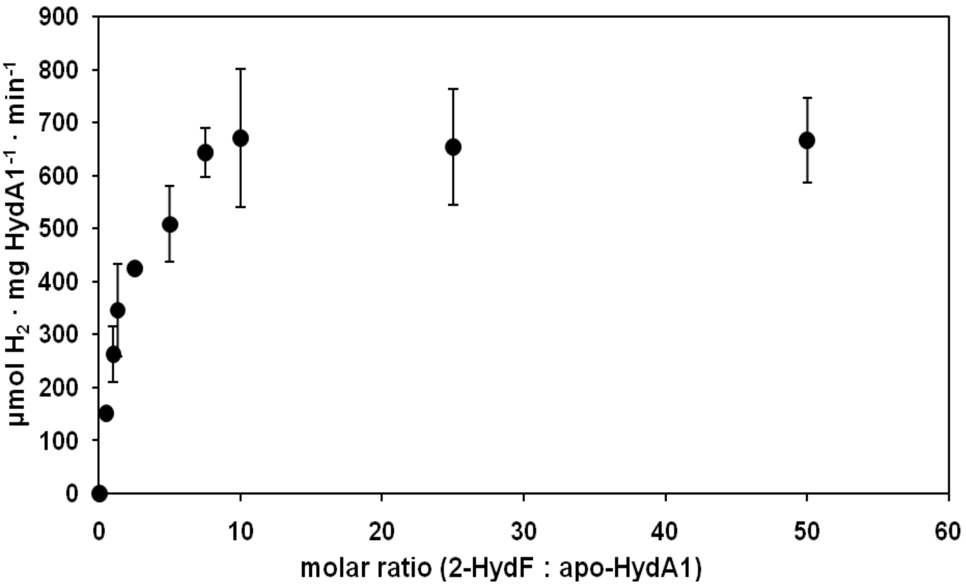

**Figure S5:** Dependence of the specific activity of HydA1 on the number of equivalents of **2**-HydF used during a 30 min transfer reaction, as described in the experimental section. Errors bars correspond to standard deviations.

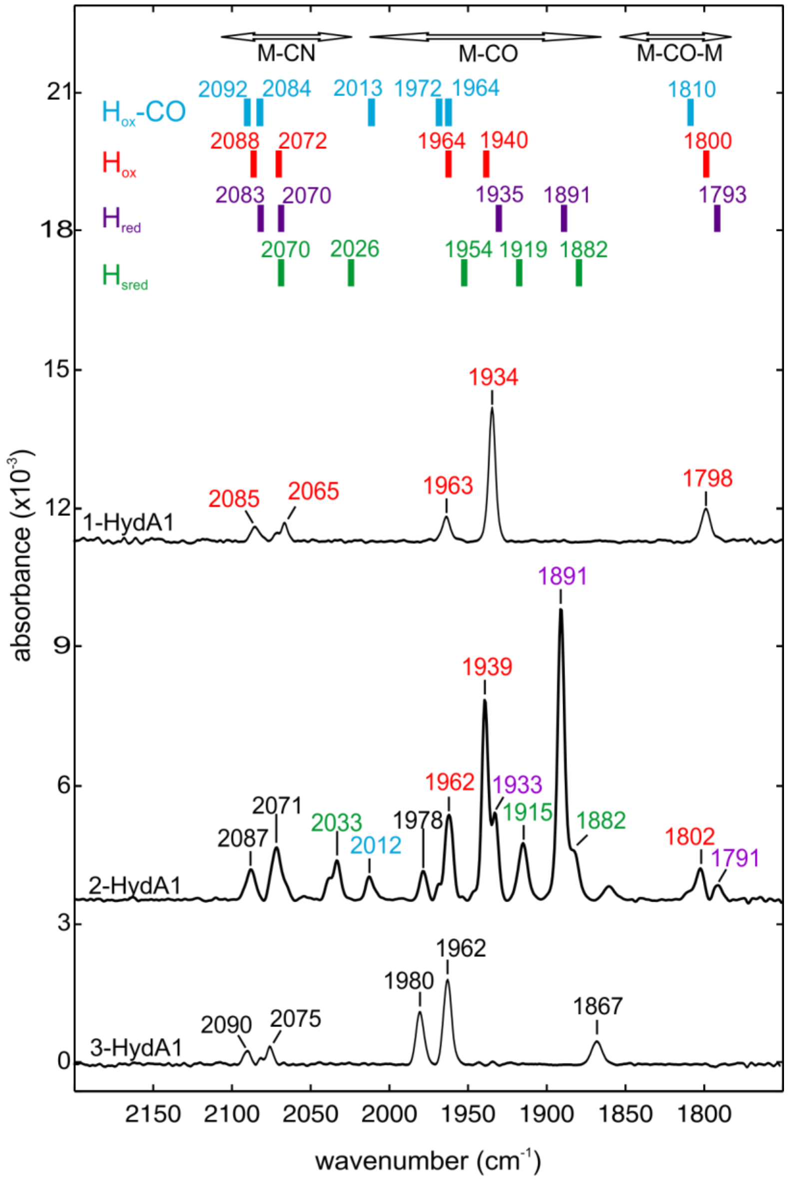

**Figure S6:** FTIR spectra recorded for HydA1 after treatment of apo-HydA1 with **1**-HydF (**1**-HydA1), **2**-HydF (**2**-HydA1) and **3**-HydF (**3**-HydA1) together with complete information on the FTIR signal positions for each redox state of native HydA1. The colour code indicates the contributions from $H_{ox}$, $H_{red}$, $H_{sred}$ and $H_{ox}$-CO ( the $H_{ox}$ state is marked in red, the $H_{red}$ state in violet, the $H_{sred}$ state in green and the $H_{ox}$-CO state in light blue).

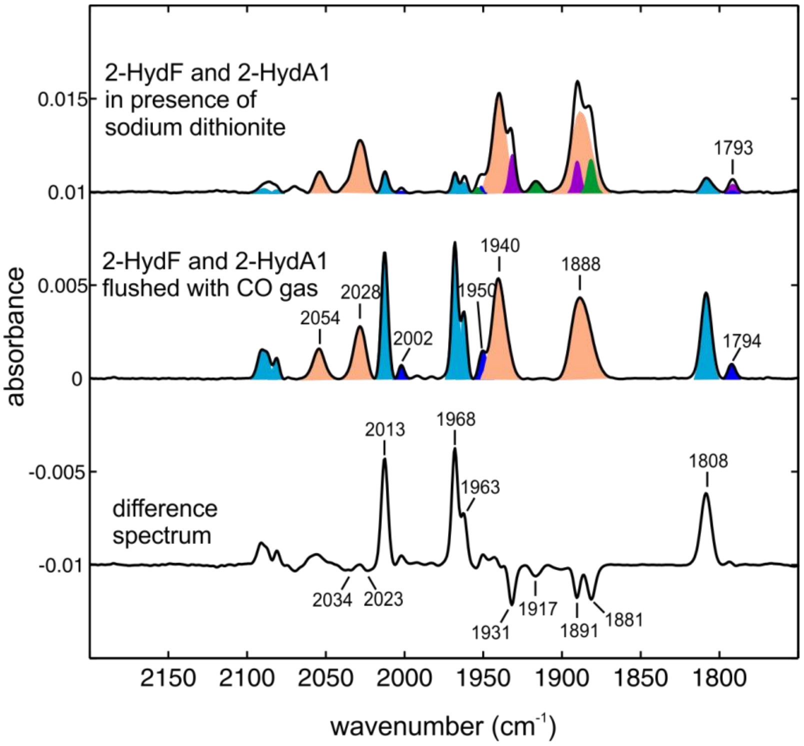

**Figure S7**. FTIR spectra of a mixture of apo-HydA1 and **2**-HydF (2-4 molar equivalents) after 60 min (top) and after additional exposure to CO gas (middle). The difference spectrum is shown at the bottom. Bands shaded in orange originate from **2**-HydF, light blue from **2**-HydA1 in the $H_{ox}$-CO state, violet from **2**-HydA1 in the $H_{red}$ state, green from **2**-HydA1 in the $H_{sred}$ state. Interestingly, additional low intensity $H_{ox}$-CO "ghost" peaks (indicated in dark blue) previously observed in heterologously expressed HydA1[5] are also visible in our preparation. The positive peaks in the difference trace represent the $H_{ox}$-CO state while the negative peaks show the positions of the $H_{red}$ and $H_{sred}$ bands.

# References

1. Seyferth, D. et al. Novel Anionic Rearrangements in Hexacarbonyldiiron Complexes of Chelating Organosulfur Ligands. *Organometallics* **6**, 283-294 (1987).
2. Song, L.C., Yang, Z.Y., Bian, H.Z. & Hu, Q.M. Novel single and double diiron oxadithiolates as models for the active site of [Fe]-Only hydrogenases. *Organometallics* **23**, 3082-3084 (2004).
3. Noodleman, L., Peng, C.Y., Case, D.A. & Mouesca, J.M. Orbital Interactions, Electron Delocalization and Spin Coupling in Iron-Sulfur Clusters. *Coordination Chemistry Reviews* **144**, 199-244 (1995).
4. Moriaud, F., Gambarelli, S., Lamotte, B. & Mouesca, J.M. Detailed proton Q-band ENDOR study of the electron spin population distribution in the reduced $[4Fe\text{-}4S]^{1+}$ state. *Journal of Physical Chemistry B* **105**, 9631-9642 (2001).
5. Velde, G.T. & Baerends, E.J. Numerical-Integration for Polyatomic Systems. *Journal of Computational Physics* **99**, 84-98 (1992).
6. Vosko, S.H., Wilk, L. & Nusair, M. Accurate Spin-Dependent Electron Liquid Correlation Energies for Local Spin-Density Calculations - a Critical Analysis. *Canadian Journal of Physics* **58**, 1200-1211 (1980).
7. Becke, A.D. Density-Functional Exchange-Energy Approximation with Correct Asymptotic-Behavior. *Physical Review A* **38**, 3098-3100 (1988).
8. Perdew, J.P. Density-Functional Approximation for the Correlation-Energy of the Inhomogeneous Electron-Gas. *Physical Review B* **33**, 8822-8824 (1986).
9. Adamo, C. & Barone, V. Toward reliable density functional methods without adjustable parameters: The PBE0 model. *Journal of Chemical Physics* **110**, 6158-6170 (1999).
10. Stephens, P.J., Devlin, F.J., Chabalowski, C.F. & Frisch, M.J. Ab-Initio Calculation of Vibrational Absorption and Circular-Dichroism Spectra Using Density-Functional Force-Fields. *Journal of Physical Chemistry* **98**, 11623-11627 (1994).
11. Szilagyi, R.K. & Winslow, M.A. On the accuracy of density functional theory for iron - Sulfur clusters. *Journal of Computational Chemistry* **27**, 1385-1397 (2006).
12. Nakamoto, K. (ed.) *Infrared spectra of inorganic and coordination compounds*, (Wiley-Interscience, 1970).
13. Stoll, H., Pavlidou, C.M.E. & Preuss, H. Calculation of Correlation Energies in Spin-Density Functional Formalism. *Theoretica Chimica Acta* **49**, 143-149 (1978).
14. Czech, I., Silakov, A., Lubitz, W. & Happe, T. The [FeFe]-hydrogenase maturase HydF from Clostridium acetobutylicum contains a CO and CN- ligated iron cofactor. *FEBS Letters* **584**, 638-642 (2010).
15. Shepard, E.M. et al. Synthesis of the 2Fe subcluster of the [FeFe]-hydrogenase H cluster on the HydF scaffold. *Proceedings of the National Academy of Sciences of the United States of America* **107**, 10448-10453 (2010).
16. Hubrich, M., Jeschke, G. & Schweiger, A. The generalized hyperfine sublevel coherence transfer experiment in one and two dimensions. *Journal of Chemical Physics* **104**, 2172-2184 (1996).